Micromotor-based localized electroporation and gene transfection of mammalian cells

Yue Wu[a,1], Afu Fu[b,1], and Gilad Yossifon[a,2]

[a]Faculty of Mechanical Engineering, Micro-, and Nanofluidics Laboratory, Technion – Israel Institute of Technology, Haifa 32000, Israel; and [b]Technion Rappaport Integrated Cancer Center, the Rappaport Faculty of Medicine and Research Institute, Technion-Israel Institute of Technology, Haifa 3109601, Israel

Herein, we studied localized electroporation and gene transfection of mammalian cells using a metallodielectric hybrid micromotor that is magnetically and electrically powered. Much like nanochannel-based, local electroporation of single cells, the presented micromotor was expected to increase reversible electroporation yield, relative to standard electroporation, as only a small portion of the cell's membrane (in contact with the micromotor) is affected. In contrast to methods in which the entire membrane of all cells within the sample are electroporated, the presented micromotor can perform, via magnetic steering, localized, spatially precise electroporation of the target cells that it traps and transports. In order to minimize nonselective electrical lysis of all cells within the chamber, resulting from extended exposure to an electrical field, magnetic propulsion was used to approach the immediate vicinity of the targeted cell, after which short-duration, electric-driven propulsion was activated to enable contact with the cell, followed by electroporation. In addition to local injection of fluorescent dye molecules, we demonstrated that the micromotor can enhance the introduction of plasmids into the suspension cells because of the dielectrophoretic accumulation of the plasmids in between the Janus particle and the attached cell prior to the electroporation step. Here, we chose a different strategy involving the simultaneous operation of many micromotors that are self-propelling, without external steering, and pair with cells in an autonomic manner. The locally electroporated suspension cells that are considered to be very difficult to transfect were shown to express the transfected gene, which is of significant importance for molecular biology research.

micromotor | electroporation | gene transfection

Delivery of molecules, such as plasmids, RNA molecules, proteins, probes, and drugs, across the cell membrane and into the cytoplasm of mammalian cells is critical for studying and manipulating gene expression, protein function, and cell activity. Many methods have been developed to overcome the physical barrier posed by the cell membrane, including chemical-based methods, such as calcium phosphate and liposome-mediated transfection; nonchemical methods, such as electroporation (1, 2) and cell squeezing (3); and viral methods, which uses viruses as gene vectors. Viral vectors are, by far, the most effective approach for gene transfection but are limited by labor-intensive processes and the risk of cytopathic effects. Synthetic lipoplexes are effective in transporting both genes and other molecules across the cell membrane. However, lipids, particularly cationic lipids, are associated with significant toxicity (4). Compared to adherent cells, cells in suspension have been shown to be more resistant to both liposome-mediated transfection and viral vector infection, largely due to a reduced attachment of the transfection reagent to the surface of the cells (5). Bulk electroporation has been used for DNA transfection in suspension cells (6) but requires strong electric fields [e.g., 8 kV/cm and 5 μs (7)], which leads to relatively low-viability rates (8).

Applying physical forces to create transient openings on the cell membrane for transmembrane delivery has shown promising potential. Dedicated microfluidic channels, developed to squeeze cells when they pass through a constrained channel, were shown to create temporary membrane openings (9, 10). A laser-assisted, microfluidic electroporation system was shown to induce pores on cell membranes by generating microcavitation bubbles that explode with the laser pulsing (11). Nanostraws (12, 13), integrated in the fluidic system, pierced the cell membrane and pumped the reagent directly into cytoplasm. Localized electroporation of a single cell can be achieved by local intensification of the electric field via nanostructures (14) or nanochannels (15–17), enabling the application of a small voltage drop. However, these fluidic systems lack the ability to target the electroporation to a specific cell.

An externally controlled manipulator can be applied to target a single cell. For example, solid carbon fiber microelectrodes (18), mounted on a micromanipulator, can be used to selectively trap and electroporate single cells. More recently, a nanotweezer (19), which consists of two closely spaced electrodes with gaps as small as 10 to 20 nm, was used to extract single molecules/organelles from living cells. However, the complexity of fabrication of electrodes with a nanometer-scale gap and the need for high-precision micromanipulators with free access from the outside to the sample, necessitating the use of an open chamber, poses significant limitations in its practical implementation, as well as when working with sterile systems.

Micromotors, also termed active or self-propelling particles, have been widely studied in drug delivery (20), detoxification (21), environmental remediation (22), immunosensing, and more (23, 24). They are actuated by either a uniform field [e.g., electric

Significance

A metallodielectric Janus particle–based micromotor system for local electroporation and gene transfection of a single mammalian cell is studied. This hybrid micromotor is magnetically and electrically propelled with magnetic steering to approach and contact a targeted cell. The targeted cell is then locally electroporated at its contact point with the micromotor, where the electric field is intensified. These Janus particles can enable the introduction of drugs and plasmids to a specific location along a single cell of irregular shape, such as neurons. Moreover, the localized electroporation results in increased cell viability, as only a small portion of the cell is experiencing an intensified electric field.

ENGINEERING

www.manaraa.com

field (25), magnetic field (26–30), ultrasound (31), hybrid (32, 33)], by fuel (34) [e.g., a catalytic (35), or chemical reaction (36)]. The inherent asymmetry of micromotors asymmetrically harvests and consumes energy, which creates a net propulsive force, even under uniform ambient conditions. Micromotor-based systems provide a simple means of targeting a single cell within closed microchambers, as they can be both propelled in a controlled manner and navigated to desired locations.
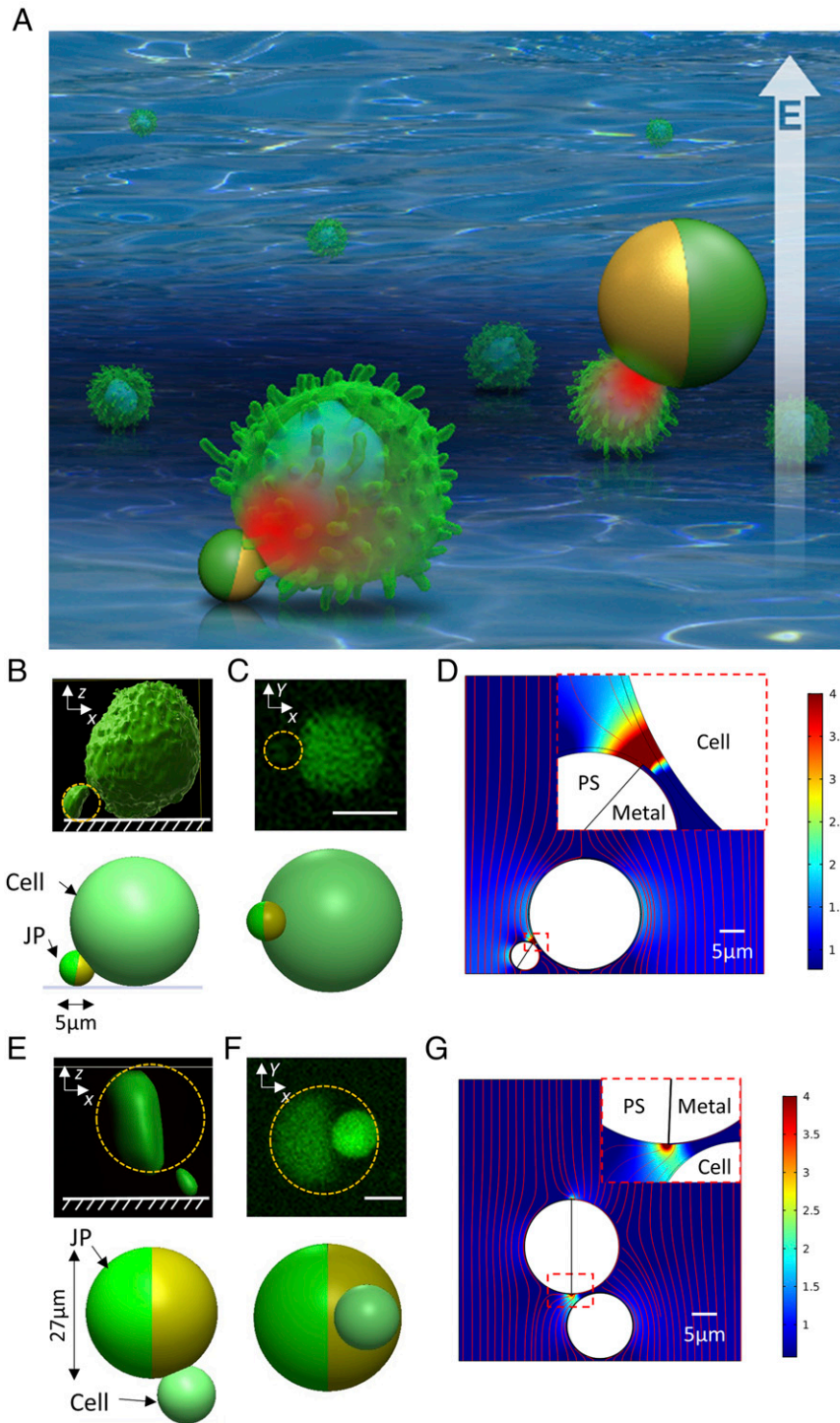

Fig. 1. Active particle system for selection and local electroporation of single-mammalian cells. (*A*) Schematics of JPs of varying sizes, used to select and locally electroporate suspension mammalian cells. Side- (*B*) and bottom-view (*C*) of a 5-μm diameter JP (yellow dashed line) attached at the upper portion of its metal-coated surface to a mammalian cell (K562). (*Upper*) Three-dimensional (3D) images constructed from z-scan images obtained with a confocal microscope. (*Lower*) Schematic presentation. (*D*) Numerical simulation of a JP (diameter: 5 μm) attached to a mammalian cell. Color plot indicates the electric field magnitude normalized by its value away from the JP. Side- (*E*) and bottom-view (*F*) of a 27-μm diameter JP (yellow dashed line) attached at the lower portion of its metal-coated surface to a mammalian cell (K562). (*Upper*) 3D image constructed from z-scan images obtained with a confocal microscope. (*Lower*) Schematic presentation. (*G*) Numerical simulation of a JP (diameter: 27 μm) attached to a mammalian cell. (Scale bar, 10 μm.)

www.manaraa.com

Different strategies of drug delivery into cells using micromotors have been demonstrated (37). For example, membranes of targeted single cells were successfully photomechanically perforated by an ultrasound-driven, gold nanoshell–functionalized, and tubular polymer nanoswimmer (31). Microneedles (26) have also been used to perforate single cellular membranes either to mechanically lyse cells or load drugs. Lipoplexes (38, 39), complexed with DNA and proteins and then physically adsorbed onto the surface of magnetically driven helical nanomotors, were proven effective in single-cell gene delivery. However, all the above-mentioned methods require separate and decoupled techniques for motor actuation, drug loading and transport, and drug delivery across the cell membrane.

Here, we demonstrate the ability to selectively electroporate a single-suspension mammalian cell using our reported electrically powered micromotor system, made of metallodielectric Janus particle (JP), that unifies (40) micromotor propulsion, cell contacting/trapping, and electroporation operations (Fig. 1A). Similar to other external fields, electric-based self-propulsion is a fuel-free approach and avoids issues of finite life (36) and/or nonbiocompatibility of commonly used fuels (35, 41). In order to minimize nonselective electroporation, far-field micromotor propulsion is obtained using magnetic rolling, while near-field self-propulsion is realized using an externally applied electric field driving via either induced charge electrophoresis (42, 43) (1 to ~10 kHz in 3 µS/cm medium) or self-dielectrophoresis (sDEP) (44) (~10 kHz to 2 MHz in 3 µS/cm medium). The interaction between the uniformly applied electric field and the JP results in a locally intensified electric field and gradients at the JP level, which, because of attractive positive dielectrophoresis (pDEP) forces, enable JP attachment to the cell. This field intensification also enables electroporation of the target cell. In contrast to the selected bacteria cell electroporation method described in our recent publication (40, 45), wherein the entire membrane of the bacteria trapped by a much larger JP is electroporated, the drug/biomolecule delivery described here involves its injection into the mammalian cell only at the point of contact between the JP (5 and 27 µm) and the cell membrane, instead of through transient pores distributed throughout the entire membrane, which minimizes damage to the cell (46) and offers spatial precision, as well as control over the timing of delivery and dose of the delivered agents (12). Moreover, by exploiting dielectrophoretic forces (47) induced by the same applied electric field, the micromotor system can load cargo in a tunable and label-free manner into the targeted cell. Demonstrated herein is the first targeted, single mammalian cell transfection system using a micromotor for local electroporation.

Results

Directed Motion-Based Approach to and Contact of a Selected Mammalian Cell by a JP.
The ability of JPs of varying diameters (5, 10, and 27 µm) to advance toward and contact a mammalian cell (K562) was studied within an experimental setup consisting of conductive indium tin oxide (ITO)-coated top and bottom glass slides (*SI Appendix*, Fig. S1). Since live K562 cells exhibit a pDEP response within sucrose media (conductivity: 3 µS/cm), at a frequency range of 1 kHz to 2 MHz, only high–electric field regions on the JP surface enabled it to advance toward and contact/trap the cell, while low–electric field regions repelled it. Only the upper portion of the metallic coating (Fig. 1 *B* and *C* and Video S1) of 5-µm diameter JPs, which exhibited a local high–electric field region (Fig. 1D), contacted the K562 cell. In contrast, 27-µm diameter JPs contacted the K562 cell via the lower portion of the metallic coating (Fig. 1 *E* and *F* and Video S2), where the local electric field was high (Fig. 1G). Because of the comparable size of 10-µm diameter JPs and the cells (17 µm), at high frequencies corresponding to sDEP motion, the JP approached the cell with its metal-coated hemisphere forward and its equator exhibiting an electric field minimum. The resulting DEP repulsion resulted in failed contact with the K562 cell (Video S3).

To avoid unnecessary and nonselective exposure of all K562 cells within the chamber to the applied electric fields, the JP was first driven to the targeted cell via a rolling magnetic field, without applying an electric field (Fig. 2 *A–C*). After the JP reached the vicinity of the targeted cell, the electric field was turned on for JP propulsion, while the magnetic field was simultaneously used to steer the JP to the cell (Fig. 2 *D* and *E*). Thus, the exposure time of all K562 cells to electric fields during JP propulsion was <10 s (Fig. 2 *F* and *G*).

Quantifying JP-Based Electroporation of Targeted Cells under Continuous AC Field.
As the electric field is enhanced at the upper (45) or lower (40) portions of the JP, cells in contact with a smaller (5 µm) or larger (27 µm) JP, respectively, experience high localized electric fields. This results in the more rapid electroporation of attached cells, as compared to nonattached cells. Fig. 3A shows that a K562 cell in contact with a 5-µm JP began to uptake propidium iodide (PI) after contact with a JP (20 kHz, 10 V, and 47 s), while the other cells showed no uptake. Fig. 3B shows that a K562 cell in contact with a 27-µm JP (white dashed line) began to uptake PI after contact with a JP (20 kHz, 10 V, and 15 s), while the other cells showed no PI signal (blue dashed line). All K562 cells in contact with 27-µm JPs began to uptake PI within less than 50 s, while 50% of cells in contact with 5-µm JPs began to uptake PI within less than 50 s, and only 14% of the noncontacted K562 cells began to uptake PI within the same time frame (Fig. 3C). This observation indicates the increased electroporation efficiency of the 27-µm JP, relative to that of the 5-µm JP (Fig. 3D). The electroporated K562 cells remained viable for at least 60 s, as demonstrated by the maintained 6-carboxyfluorescein diacetate (CFDA) fluorescence intensity, in all cells.

Visualizing the Local Injection of Molecules into Cells Following Localized Electroporation.
Because of the pDEP response of the cells, their point of contact with the JP corresponds to the locations on the JP surface wherein the electric field is intensified and where the cell membrane is subsequently electroporated. Fig. 4A shows sequential microscope images of PI staining of a K562 cell, following injection of the dye through the point of contact with a 5-µm JP. The PI staining propagated from the region near the point of contact with the JP to more distal regions (Fig. 4 *A* and *B*). In contrast, when the normalized fluorescence intensity reached 42% of its maximal value obtained for a cell attached with 5-µm JP at 100 seconds under 20 kHz and 10 V (see *Materials and Methods* for details on the normalization procedure), the central part of the cell displayed the highest fluorescence intensity, which may have been due to preferential PI binding to DNA in the nucleus of the cell. Similar PI uptake kinetics were found in cells bound to 27-µm JPs (Fig. 5).

Average staining time, defined as the time between reaching 10 to 15% and 42% intensity, was shorter in cells bound to 27-µm JPs as compared to those attached to 5-µm JPs (Fig. 5C). The enhanced uptake may have partially resulted from the induced electroosmotic flow around the JP (48), which pumps the fluorescent dye into the cell. Thus, the larger the JP, the higher the electroosmotic flow. PI staining from 10 to 42% of nonattached K562 cells required significantly longer durations of time (47 ± 26 s), as compared to those bound to 27- or 5-µm JPs (P = 0.033 and 0.1504, respectively) (Fig. 5C). Besides electroporation of cells that are located beneath the 27-µm JP (see Fig. 1 *E* and *F*), cells that are adjacent to the JP could also be electroporated by contacting its metallodielectric interface (*SI Appendix*, Fig. S2).

Controlling Molecule Delivery into Living Cells Using a JP and an AC Pulse.
When using a train of two AC pulses (10 kHz and 20 V) for JP-assisted, reversible electroporation (Fig. 6A), pulse widths of
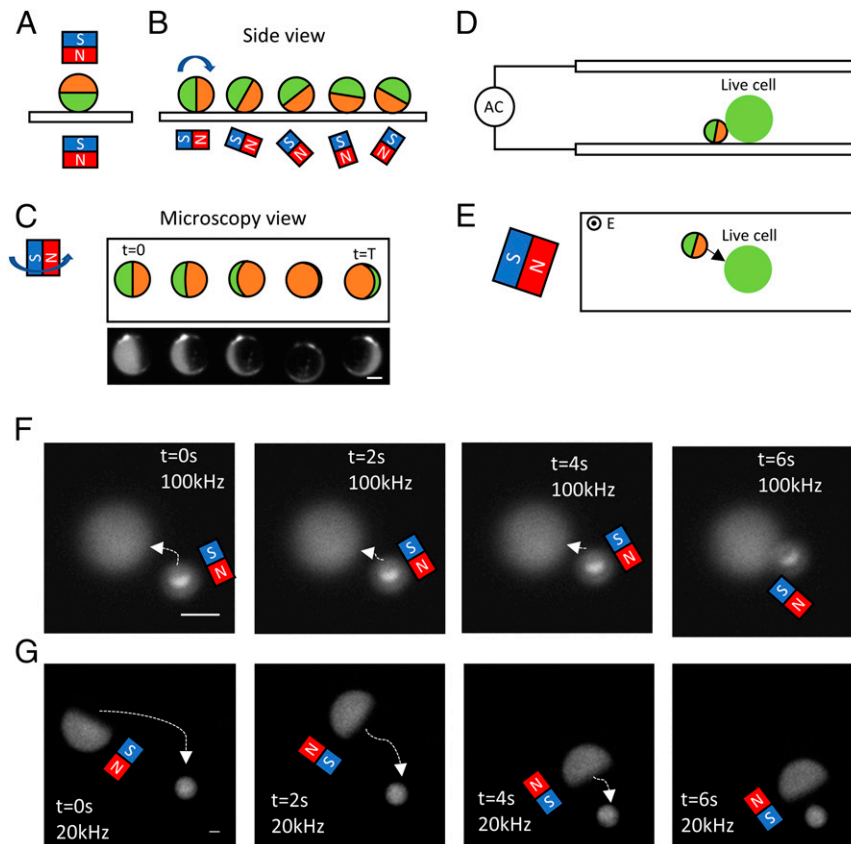
Wu et al.
Micromotor-based localized electroporation and gene transfection of mammalian cells

PNAS | 3 of 12
https://doi.org/10.1073/pnas.2106353118

www.manaraa.com

Fig. 2. Methodology of propelling and steering a JP particle to a mammalian cell (K562). (*A*) Magnetization of the JP. (*B*) Schematic side view and (*C*) inverted microscopy view of a rolling JP, induced by a rotating magnetic field, without application of an electric field. (*D*) Schematic side view and (*E*) inverted microscopy view of a JP approaching a mammalian cell by electric propulsion and magnetic steering. (*F*) Sequential images of a 5-μm JP approaching and contacting a K562 cell, under 100 kHz and 7 V. (*G*) Sequential images of a 27-μm JP approaching and contacting a K562 cell, under 20 kHz and 10 V. (Scale bar, 10 μm.)

25, 37.5, and 50 ms resulted in maximum PI signals of 2.85, 3.67, and 15.78% of the signal intensity obtained for a pulse width of 62.5 ms and 20 V at 360 s (see *Materials and Methods* for normalization procedure), respectively (Fig. 6 *B* and *C* and Video S8). At the same time, the CFDA intensity was >20% of its initial value. In contrast, at a pulse width of 62.5 ms, the PI signal continued to increase within the examined time window. At pulse widths exceeding 62.5 ms, the cell bound to the JP was electrically lysed and ruptured (Video S9). The amount of molecules introduced into the targeted living cell using the 27-μm JP was controlled (Fig. 6 *B–D*) and was significantly higher than the amounts of PI delivered into cells not bound to 27-μm JPs ($P = 0.028$, 0.01, 0.078, and 0.015 for 25, 37.5, 50, and 62.5 ms, respectively). Taken together, the amount of injected molecules (PI) can be controlled by varying the pulse duration.

To demonstrate the applicability of our system to adherent cells of irregular shape, we examined the local electroporation of a neuron cell. As seen in Fig. 7 (Video S8), a JP (27 μm) first approached a targeted neuron cell using rotating magnetic field followed by electrical propulsion to contact the cell at the desired location with its metallic-coated side and then to locally electroporate and inject PI into the cell. The rotating magnetic field was turned on between 4 and 30 s. From 30 to 95 s, an electric field of 100 kHz and 10 V was turned on for JP propulsion and contacting of the neuron cell at the desired location. At 120 s, the AC pulse was turned on (2 AC pulses, 10 kHz, and 20 V; pulse width: 10 ms). In between these two pulses, 1 MHz and 10 V was applied to maintain contact, via DEP force, between the cell and the JPs' metallic side. Fluorescent intensity of the

injected PI was clearly seen at 156 s below the metallic side of JP. At 180 s, a clear staining of the nucleus PI was observed. A similar approach of a neurite (PC-12) by JP (27 μm) was demonstrated in *SI Appendix*, Fig. S3.

Preconcentration and Targeted Transfection of Plasmids by the JP. The JP can increase transfection efficiency by trapping and accumulating plasmids while locally electroporating the cell (Fig. 8*A*). The active particle (i.e., JP) traps and accumulates the plasmids (FUGWm) onto its surface due to the pDEP response of the plasmids (49). In general, smaller cargos are trapped between the metallic surface of the JP and the ITO substrate, where electric fields are locally intensified. Fig. 8*B* and Video S7 show the time lapse of navigation and trapping of plasmids (FUGWm) using a mobile 27-μm JP, under 100 kHz and 5 V within a 300 mM sucrose medium, conditions under which the plasmids exhibit a pDEP response (Video S7). Cargo can then be released by simply turning off the electric field.

The electroporation process consisted of two steps: 1) driving of the JP at 100 kHz and 10 V for 1 to 2 min to trap the plasmids and pair the JP with a K562 cell (see Fig. 8*A* and Video S7). In this step, the collected green fluorescence protein (GFP)–encoding plasmids were either trapped in between the K562 cell under the JP (Fig. 8*C*) or brought into close vicinity of the K562 cell, which was in contact with the polystyrene (PS) side of the JP or with its metallodielectric interface. 2) Electroporating the paired cell using a single DC pulse of 5 V of 0.5 ms duration. Successful electroporation of K562 cells was demonstrated by GFP expression after an incubation time of 18 h (Fig. 8*D*).
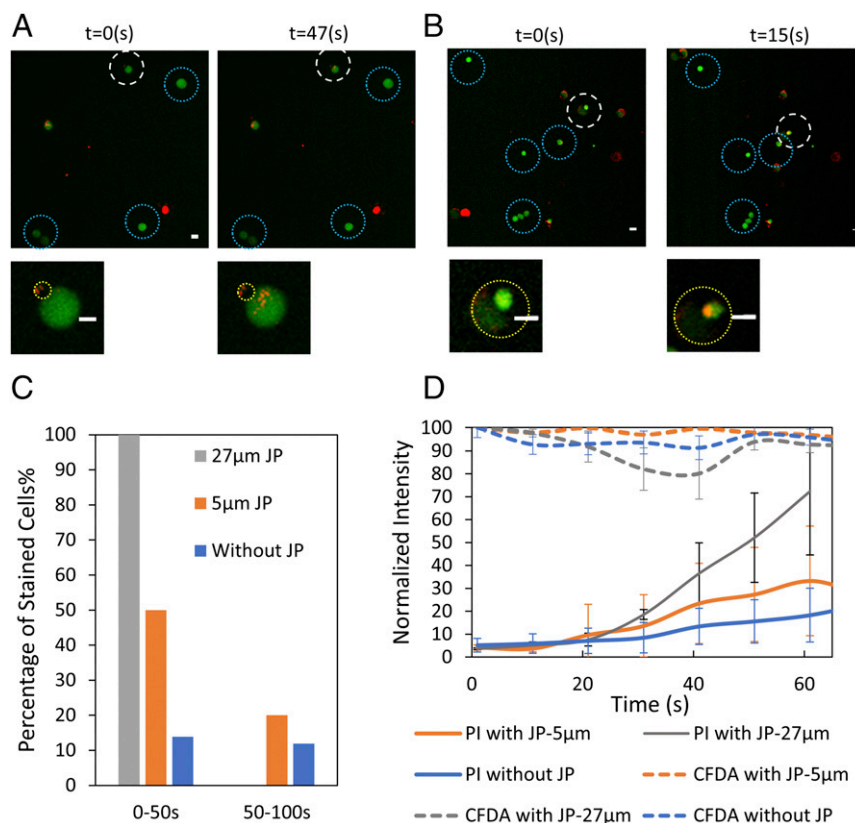
www.manaraa.com

Fig. 3. JP-driven, directed K562 cell electroporation under a continuous AC field (20 kHz and 10 V) and maintained cell viability. Confocal microscopy view of a JP [diameter: 5 μm (*A*) (Video S4) and diameter: 27 μm (*B*) (Video S5)] attached (white circle) versus nonattached to a K562 cell (blue circle), with PI (red fluorescence) and CFDA (green fluorescence) channels superimposed at various times of electric field operation. (*C*) The percentage of PI-stained cells at various time points of field operation, in the presence and absence of JPs. Of note, a PI intensity increase of ~10 to 15% is considered a stained cell. (*D*) Normalized PI and CFDA intensity in cells attached versus nonattached to JPs (see *Materials and Methods* for details on the normalization procedure). (Scale bar, 10 μm.)

Fig. 8*E* shows that the chamber with JPs had a higher transfection rate (8.77%) than the chamber without JPs (1.03%). The viability of our system was found to be above 95% (*SI Appendix,* Table S1 and Fig. S4).

To summarize, JPs increased transfection rates by their dual effect of bringing more plasmids into close proximity with the cell and locally increasing the electric field intensity. In the experiments detailed in the *Visualizing the Local Injection of Molecules into Cells Following Localized Electroporation* section, 27-μm JPs locally intensified the electric field at the point of contact with the K562 cell (Fig. 5*A*), which resulted in the injection of PI into the cell. Together, with the JP-driven increase in plasmid concentrations near the electroporated cell (e.g., Fig. 8*C*), the presented micromotor system brought to enhanced transfection rates.

Discussion

This work demonstrated the ability to inject molecules (e.g., PI) into a targeted mammalian cell through the contact point between a JP and an attached cell, thereby achieving spatially controlled delivery at a single-cell level. This was achieved by applying either a continuous AC electric field or a train of AC pulses. Finally, the active particle system efficiently introduced DNA molecules into targeted K562 cells upon the application of a DC pulse, without impacting cell viability.

The relatively low transfection efficiency (8.8%) seems to be related to the low percentage of cells that were paired (i.e., in contact) with JPs (maximum of 19.3%; *SI Appendix,* Fig. S5). The low number of JP–cell pairs was because of several reasons. First, only cells that are smaller in diameter (<15 μm) than the JP (27 μm)

could be trapped between the ITO substrate and the metallic surface of the JP. Larger cells (15 to 20 μm), comparable in size to the JP, were repelled by the metallic-coated side of the JP, in which a local electric field minimum exists because of the negative dielectrophoretic (nDEP) forces. This can be improved by using a JP larger than 27-μm. Second, increasing the concentration of the JPs can increase the pairing percentage until its saturation (~19.3%) due to interactions between the JPs forming clusters/chains. Improving the mobility of the electrically propelled JPs while reducing their adsorption on the substrate will increase their chances to pair to a cell, which, in turn, can increase the pairing percentage.

According to the literature, using low-conductivity electroporation medium increases the cell viability (50) and transfection effectiveness (51–54) under electroporation operation. G. Pucihar (50) showed that the increased cell viability in low-conductivity solution is due to decreased heating. Without an applied electric field, the sucrose buffer (300 mM sucrose) used in this study is not affecting the cell viability. The buffer used in our study is able to maintain 87% cell viability within 1 h (*SI Appendix,* Fig. S6). All the experimental processes, including exchanging buffer of cells, loading into the chamber, and electroporation tests, were completed within 1 h.

In conventional electroporation, different electric field strength and electroporation medium generate different transfection efficiency, which varies from 5 (55) to 40% (56) (*SI Appendix,* Table S2). The viability also varies from 10 (55) to 80% (57). Several recent literatures on microfluidics-based electroporation for K562 are also listed in *SI Appendix,* Table S2. The transfection efficiency varies from 13 (58) to 76.2% (57). The viability is higher than the
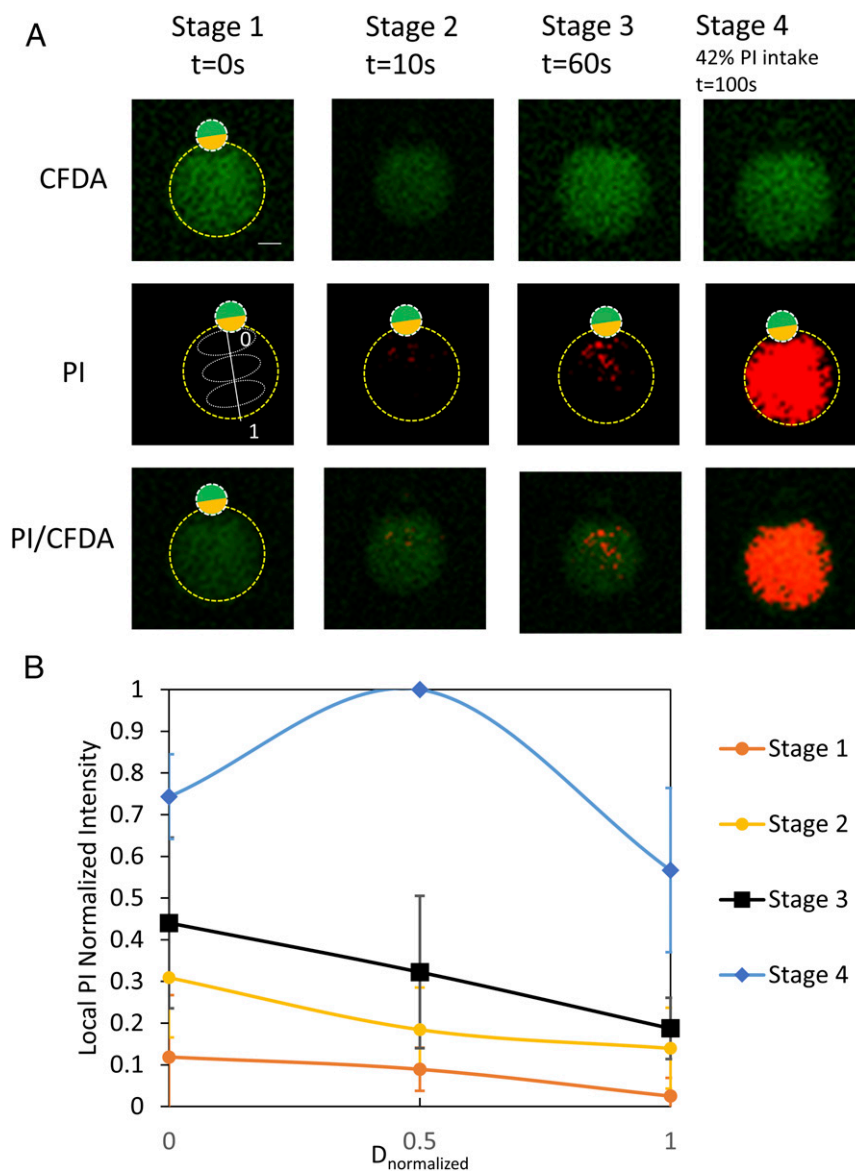
ENGINEERING

www.manaraa.com

Fig. 4. Localized, reversible, and JP-induced electroporation under continuous AC field (20 kHz and 10 V), as observed through the injection of PI into a K562 cell at its point of contact with a 5-μm JP. Confocal microscopy image of PI (red), CFDA (green), and PI/CFDA channels (*A*) (Video S6) and corresponding fluorescence intensity profiles (*B*), along the direction of injection normal to the JP–cell contact interface, at different time points of the injection process. Stages 1, 2, 3, and 4 correspond to 0, 10, 60, and 100 s from the time of electric field application. Stage 4 also corresponds to the normalized intensity reaching 42%. The regions of interest (white ellipses) for the measured intensity are marked in *A*. (Scale bar, 5 μm.)

conventional electroporation method [from 65 (59) to 80% (57)]. Although our JP system did not increase the transfection efficiency, compared with most of the conventional and microfluidic electroporation system, the viability was increased. The viability of the JP-based system was similar to Lentivirus-based transfection (98.9%). It is important to reemphasize the unique advantage of our JP system over these other electroporation systems in its ability to work not only as a swarm of JPs, interacting with many cells, but also as a single or few JPs that are able to target specific cells and locally electroporate the cells in any desired location along the cell body, as described in the *Controlling Molecule Delivery into Living Cells Using a JP and an AC Pulse* section and Fig. 7 for neuron cells.

One of the advantages of the use of active particles in this context lies in their ability to induce localized electroporation without the need to fabricate micro/nanogap electrodes or structures. As

reported in the literature, electrode gaps, which are smaller than the cell size, retain cell viability (46), since the high electric fields are localized. As a result, a lower uniformly applied voltage difference across the chamber is sufficient for cell permeabilization. In the presented active particle system, the localized electric field is generated by the metallodielectric JP, which does not require a complex fabrication process as compared with micro/nanogap electrodes.

Another advantage of the active particle system is the ability to spatially control electric field intensification on a single-cell level and to target a specific cell in vitro while navigating toward it. These features can enable drug introduction to a specific location along a single cell of irregular shape, such as neurons. For example, Alzheimer's disease is caused by abnormal levels of a protein, which aggregates to form plaques on the axon (60) of a neuron; Parkinson's disease is caused by aggregates of α-synuclein,
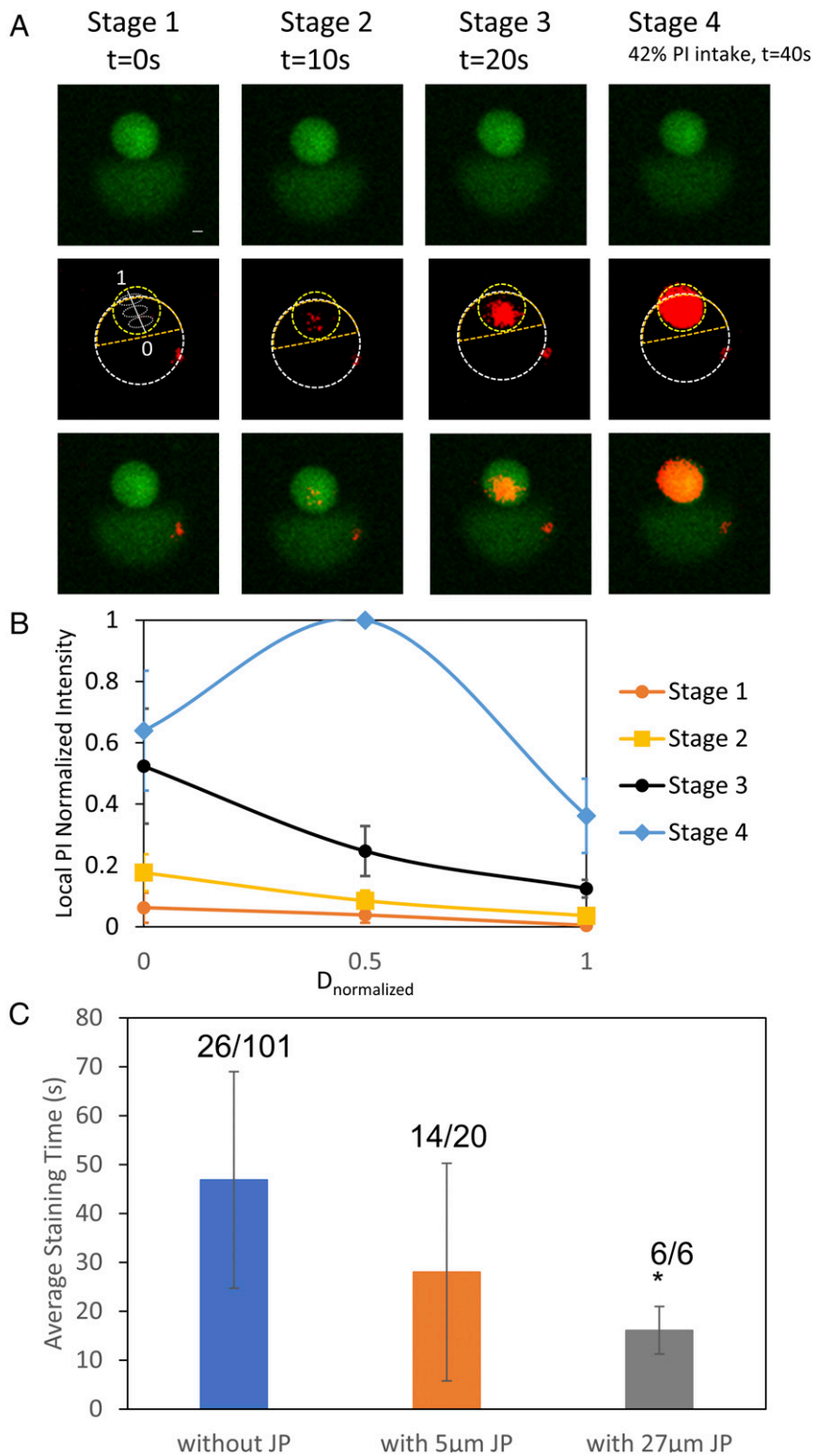
www.manaraa.com

Fig. 5. Localized, reversible, and JP-induced electroporation under continuous AC field (20 kHz and 10 V), as observed through the injection of PI into the K562 cell from its point of contact with the 27 μm JP. Confocal microscopy view of PI, CFDA, and PI/CFDA channels (*A*) (Video S7) and corresponding PI fluorescence intensity profiles (*B*) along the direction of injection normal to the JP–cell contact interface for different time stages of the injection process. The regions of interest for the measured intensity are marked in *A*. Stages 1, 2, 3, and 4 correspond to 0, 10, 20, and 40 s from the time of electric field application. Stage 4 also corresponds to the normalized intensity reaching 42%. (*C*) The average staining time (the time of PI increases from 10 to 42%) for cells with/ without contacting JPs. The number of cells that were stained versus the total number of cells in the experiments is marked above the bars. (Scale bar, 5 μm.)
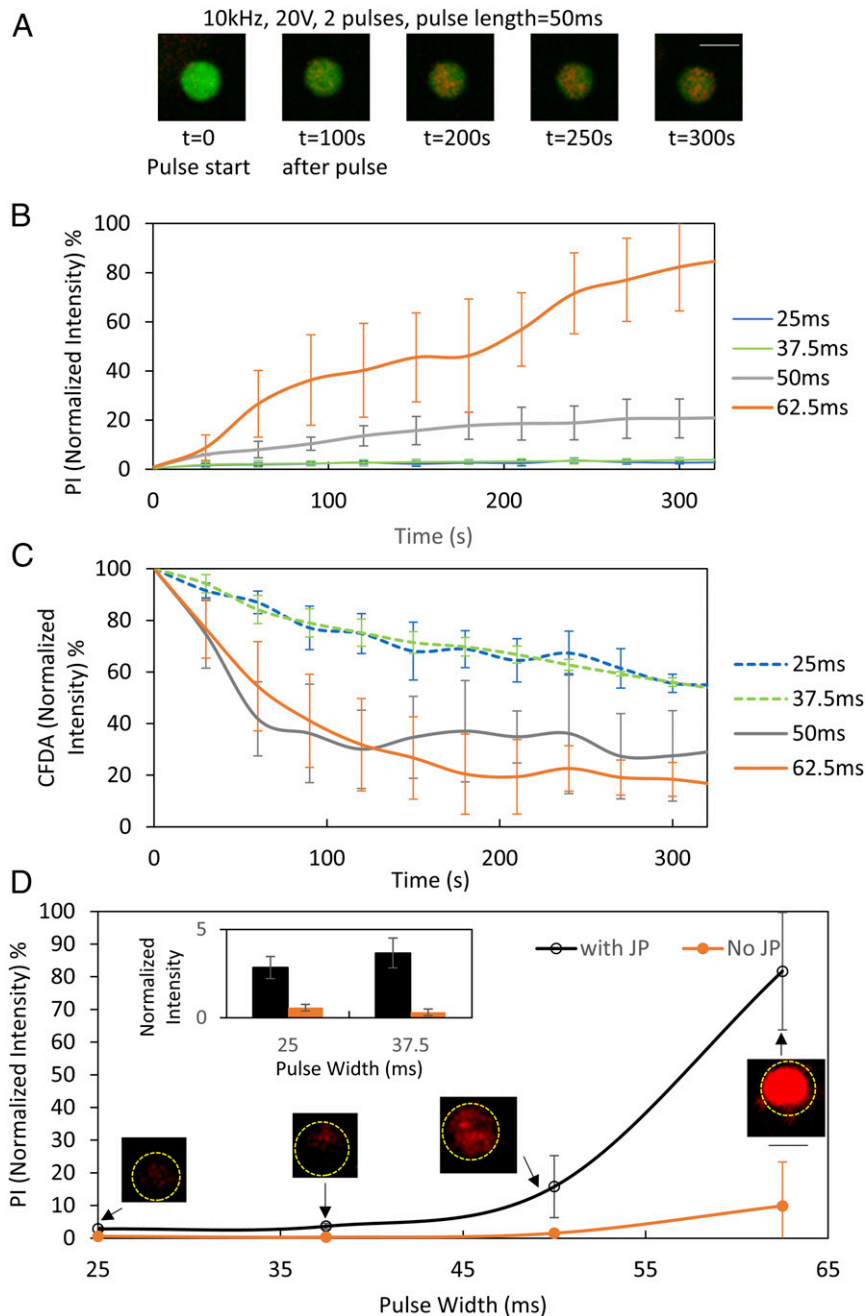
Fig. 6. JP-driven, reversible electroporation, under varying electric pulse widths, for precise control of the amount of injected PI. (*A*) Fluorescence micrographs of a cell bound to a 27-μm JP (Scale Bar, 30 μm) at different times after the application of the two AC pulses (10 kHz, 20 V, 2 pulses, and 50 ms). Normalized fluorescence intensity of PI (*B*) and CFDA (*C*) in K562 cells electroporated by 27 μm JPs subjected to two AC pulses of various durations (25 to 62.5 ms). The AC pulse train was applied at time 0. (*D*) Fluorescence intensity (PI) of cells bound/nonbound to a 27-μm JP, 360 s following the application of an AC pulse train (10 kHz, 20 V, and 2 pulses) of varying durations. The inset images show the corresponding micrographs of the cell in the PI channel taken 360 s after the pulse. (Scale bar, 15 μm.) (*Inset*) Enlarged view of the normalized PI intensity following short pulse durations (25 and 32.5 ms) in cells bound/nonbound to a JP. The time interval between the two pulses was 1 s, and these were modulated onto a continuously applied 1-MHz and 5-V field.

which accumulate in presynaptic terminals of a neuron (61); and Huntington's disease is associated with mutant huntingtin (HTT) proteins found in various locations in the neuron (62). The delivery of drugs or compounds developed to target these proteins [e.g., HTT-LC3 linker compounds reduce mutant HTT protein levels (63)] can be targeted to these specific sites of accumulation. Such an ability to approach specific parts of the neuron cell and perform local electroporation was demonstrated for both the neuron cell (Fig. 7) and even its neurite (*SI Appendix,* Fig. S3).

The ability to both trap and release gene-bearing plasmids is another advantage provided by the presented active particle-based system. While gene delivery by micromotors and nanomotors has been demonstrated before (38, 39, 64, 65), in these studies, the plasmids were permanently attached to the micromotors, rendering it impossible to release them. Furthermore, to deliver the gene, the micromotor had to be injected into the target cell (38), which required the micromotor to be of nanometer scale and to be comprised of biocompatible material or to
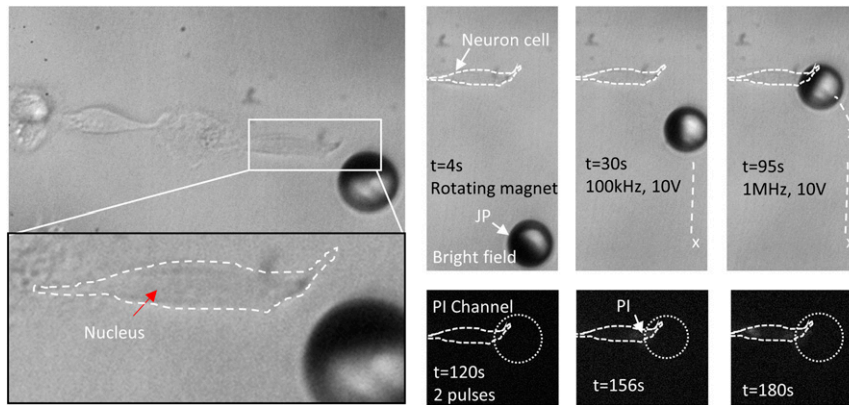
www.manaraa.com

Fig. 7. Sequential approach of a JP (27 μm) toward a targeted neuron cell (U87) by rotating the magnetic field followed by an electrical propulsion to contact the cell at the desired location and then to locally electroporate and inject PI into the cell.

have a sharp tip (<50 nm) (65) to enable the penetration of the cell membrane. Our active particle-based, and localized electroporation system concentrates the plasmids by dielectrophoresis and electroporates the cell membrane by the application of a locally intensified electric field, thereby enhancing the transfection probability, as the plasmids are accumulated exactly where the membrane is prorated. Dielectrophoresis has been found to be an efficient way to collect (66, 67) and separate (68) DNA molecules, which can then be released by simply turning the field off or, if possible, to rely on the nDEP response of the cargo. Our active particle-based system is a demonstration of a unified approach, wherein plasmid trapping and release, and its introduction into the target cell is singularly controlled by a single electric field. The platform is expected to open up possibilities for drug delivery and transfection into individual targeted cells at unprecedented spatial precision and increased efficiency and selectivity.

Materials and Methods

Magnetic JP Fabrication. PS particles (diameter: 10 μm) (Sigma-Aldrich) in isopropanol were pipetted onto a glass microscope slide, to form a monolayer of particles upon solvent evaporation. The glass slide was coated with 15 nm Cr, followed by 50 nm Ni and 15 nm Au, as described in the protocol outlined by Pethig (69) and Wu et al. (70). To magnetize the JPs, the substrates were placed in between two neodymium magnetic blocks (14 × 12 × 19 mm in size), with opposite dipoles facing each other. Next, the substrate was sonicated in deionized (DI) water with 2% (volume/volume) Tween 20 (Sigma-Aldrich) to release the JPs. The JPs were washed three times in DI water with 300 mM sucrose before the experiment.

Magnetic Steering of Janus Particles. JPs were guided by placing a neodymium magnet block (14 × 12 × 19 mm in size) at a specific orientation close to the microchamber (*SI Appendix*, Fig. S1C). The magnet was maintained at a horizontal distance of 3 cm from the focus of the objective and at the same height as the microchamber. In this setup, the magnet produced a 125 Gauss field.

Cell Culture and Preparation. Human myelogenous leukemia cell line K562 was grown at 37 °C, 5% volume/volume CO_2 and passaged every 3 d. The culture medium consisted of RPMI 1640 (Biological Industries), supplemented with 10% volume/volume heat-inactivated fetal bovine serum (FBS), 1% volume/volume penicillin-streptomycin (Biological Industries), and 2% volume/volume L-glutamine (Biological Industries). Before the experiment, the cells were incubated with 0.15 mg/mL CFDA (Sigma-Aldrich) in culture medium (37 °C, 10 min). Then, they were washed three times with 300 mM sucrose. PI (Sigma-Aldrich) was added to the cells to a final concentration of 100 μg/mL. To test the cell viability in sucrose medium and phosphate-buffered saline (PBS, 1×), K562 cells were cultured in 300 mM sucrose and PBS for 5, 10, 30, and 60 min. The cell viability was detected by a Vi-CELL XR Cell Viability Analyzer (Beckman Coulter) based on a trypan blue dye exclusion method. In each condition and time point, 50 images were captured and a total number

of more than 2,500 cells were analyzed. Cell viability was calculated automatically by the Vi-CELL XR 2.04 software.

Rat neuronal cell line PC-12 was purchased from American Type Culture Collection, and the human neuronal cell line U-87 were supplied by Prof. Ben Maoz in Tel Aviv University (TAU), Israel. PC-12 cells were cultured in RPMI 1640 medium containing 10% volume/volume heat-inactivated horse serum, 5% volume/volume heat-inactivated FBS, 1% volume/volume penicillin-streptomycin (Biological Industries), and 2% volume/volume L-glutamine (Biological Industries). U-87 cells were cultured in Dulbecco's modified eagle medium (Biological Industries), supplemented with 10% volume/volume heat-inactivated FBS, 1% volume/volume penicillin-streptomycin (Biological Industries), and 2% volume/volume L-glutamine (Biological Industries). Both cell lines were grown at 37 °C, 5% volume/volume CO_2 and passaged every 3 d. PC-12 cells were infected with an FUGWm lentiviral vector to express GFP fluorescence. The cells were seeded into the electroporation chamber 7 d before the experiment. To stimulate the neurite outgrowth, the culture medium was replaced with a complete medium containing 200 ng/mL recombinant human neuron growth factor (Sigma).

Overexpression of GFP in PC-12 and K562 Cells by Lentivirus Transduction. A GFP gene was introduced into PC-12 and K562 cells through lentivirus transduction. Briefly, a GFP-expressing FUGWm vector was cotransfected with ΔNRP and VSVG plasmids into the human embryonic kidney 293FT cells using the Calfectin reagent to produce lentivirus particles. After 48 h, supernatants containing lentivirus particles were collected and filtered with 0.45-μm filters. In each well of 6-well plate, 1 mL lentivirus supernatant and 1 mL fresh medium containing 10 μg/mL polybrene were added. After overnight incubation, cells were replaced with fresh medium. A stable cell line PC-12-GFP was generated for the following studies.

Experimental Setup. The experimental chamber consisted of a 120-μm high, silicone reservoir (Grace-Bio), sandwiched between an ITO-coated, 1-mm glass slide (Delta Technologies) and an ITO-coated coverslip (SPI Systems), as illustrated in Boymelgreen et al. (44) (*SI Appendix*, Fig. S1). Two inlet holes (~1 mm in diameter) were drilled through the top 1-mm thick ITO slide, forming a microchamber surrounded by a silicone reservoir (2 mm in height and 9 mm in diameter) filled with solution to ensure the chamber remained wet and to enable the addition of the solution with the JPs, bacteria, fluorescent dyes, and tracer particles into the channel via manual pumping. An AC electrical field was applied using a signal generator (Agilent 33520A) and monitored by an oscilloscope (Tektronix-TPS-2024). An AC pulse signal was applied using a signal generator (TTi TGA 12104 series) with multiple channels. A home-made switch (Solid State Relays [AQV252G] controlled by Arduino Nano) was used to control the duration and timing of AC pulses.

Experimental Setup for Transfection. The electroporation chamber was the same as described in the *Experimental Setup* section. The electroporation chamber contained 200 to 300 K562 cells, 2-μL plasmid (FUGWm, 600 ng/μL), and 8 μL 300 mM sucrose medium and, in relevant samples, was supplemented with at least 100 JP of 27 μm diameter. Electroporation was achieved by driving the JP at 100 kHz and 10 V (peak to peak), for 1 min, to trap the plasmids and approach K562 cells. Thereafter, a single 0.5 ms and 5 V DC pulse
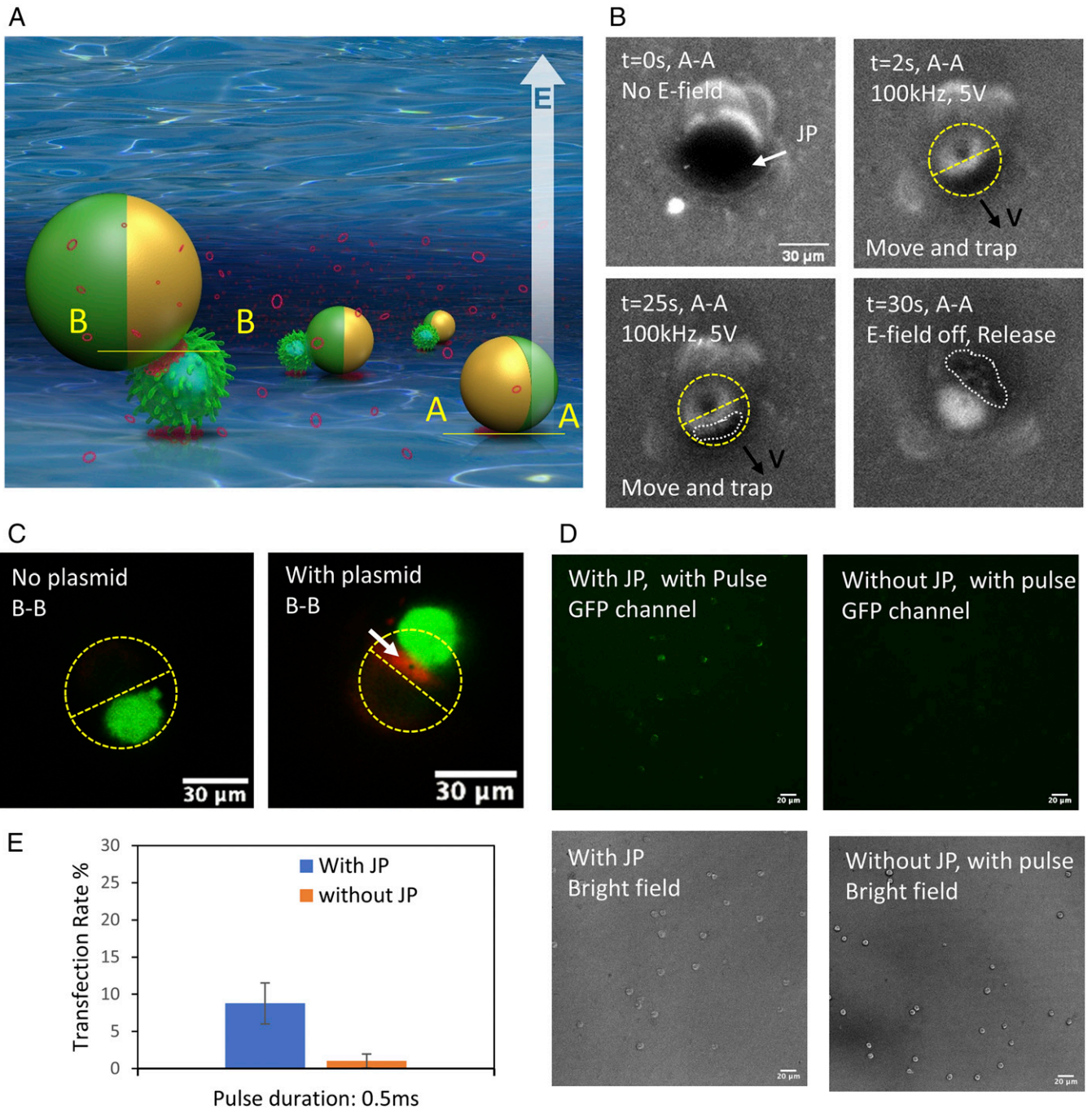
Wu et al.
Micromotor-based localized electroporation and gene transfection of mammalian cells

PNAS | 9 of 12
https://doi.org/10.1073/pnas.2106353118

Fig. 8. Transfection of plasmid into a K562 cell by a 27-μm JP using a single 0.5-ms and 5-V pulse. (*A*) Schematics of active particles that accumulate GFP-encoding FUGWm plasmids, while locally electroporating mammalian cells at different contact points (i.e., at the top of the cell and under the metallic coating), with the PS side or with the metallo–dielectric interface contacting the cell. (*B*) Sequential plasmid trapping by the moving JP (27 μm). (*C*) Confocal microscopy view at an optical sectioning plane B–B with a JP with/without plasmids (1 MHz and 10 V), located on top of a K562 cell. The trapped plasmids are marked by a white arrow. (*D*) GFP expression measured in K562 cells 18 h after electroporation with/without JPs. (*E*) The average transfection rate of plasmids in an electroporation chamber with/without JPs, as measured in three independent experiments.

was applied. Following electroporation, the sample was taken out of the chamber, placed into a culture dish with culture medium, and incubated for 18 h before transfection rate was assessed.

Selective Attachment of a Janus Particle to a Mammalian Cell and Its Local Electroporation. JPs were attached to target mammalian cells in the ITO chamber (100 kHz and 10 V), after which the electrical field parameters for electroporation were changed to either a continuous field of 20 kHz and 10 V or to AC pulses of 10 kHz and 20 V of varying durations (Fig. 6). These

electrical signals were modulated onto a continuously applied AC signal with frequency of 1 M Hz and 5 V for trapping purposes.

Microscopy and Image Analysis. Trapped and untrapped cells were observed using a Nikon Eclipse Ti-E inverted microscope equipped with a Yokagawa CSU-X1 spinning disk confocal scanner and Andor iXon-897 EMCCD camera. The chamber was placed with the coverslip side down, and images were taken using a ×20 lens. CFDA and PI fluorescent dyes were observed with lasers of wavelength 488 and 561 nm, respectively.

www.manaraa.com

Table 1. Parameters used for the calculation of K562 transmembrane potential under various conditions

Parameter	Meaning	Continuous AC electroporation (20 kHz, 10 V)	Continuous AC trapping without motion (1 MHz, 5 V)	Continuous AC field for approaching and contacting cells using 5 μm JP (100 kHz, 10 V)	Pulsed AC electroporation (10 kHz, 20 V)
E_{appl} (V/cm)	Applied field strength	833.3	416.65	833.3	1,666.6
f (Hz)	Frequency	20×10^3	1×10^6	1×10^5	10×10^3
ω (rad/s)	$2\pi f$	1.26×10^5	6.28×10^6	6.28×10^5	6.28×10^4
a (cm)	Radius of the cell	1×10^{-4}	1×10^{-4}	1×10^{-4}	1×10^{-4}
C_{membr} (F/cm^2) (71)	Capacitance of the membrane	0.9×10^{-6}	0.9×10^{-6}	0.9×10^{-6}	0.9×10^{-6}
ρ_{int} (Ω cm)	Resistivity of the internal fluid	454.55	454.55	454.55	454.55
ρ_{ext} (Ω cm)	Resistivity of external medium	1.38×10^5	1.38×10^5	1.38×10^5	1.38×10^5
τ (μs)	Relaxation time of membrane	10.6	10.6	10.6	10.6
$\Delta\psi_{membr}$ (V)	Transmembrane potential	0.159	0.0016	0.0478	0.472

Normalization. The PI fluorescence intensity level in Fig. 3D was normalized according to $(I_t-B_0) / (I_{60}-B_0) \times 100$, wherein I_t and B_0 are the average PI fluorescent intensity of the cell at time t and that of the background at time t = 0, respectively, while I_{60} stands for the maximum average intensity achieved for the cells that were attached to a 27-μm JP at 60 s under 20 kHz and 10 V. In the CFDA channel, the fluorescence intensity was normalized according to $(I_t-B_0) / (I_0-B_0) \times 100$, wherein I_t and B_0 are the average CFDA fluorescent intensity of the cell at time t and that of the background at time t = 0, respectively, while I_0 stands for the initial t = 0 s of the CFDA average intensity of the cell under measurement.

In Figs. 4B and 5B, the fluorescence intensity was normalized according to $(I_i^s-B_0^1) / (I_{0.5}^4-B_0^1) \times 100$, wherein I_i^s and B_0^1 are the average PI fluorescent intensity of location i (0, 0.5, or 1) within the electroporated cell at stage s and location 0 at stage 1, respectively, while $I_{0.5}^4$ stands for the maximum average intensity achieved within location 0.5 at stage 4.

In Fig. 6, the PI fluorescence signal was normalized according to $(I_t-B_0) / (I_{360}-B_0) \times 100$, wherein I_t and B_0 are the average PI fluorescent intensity of the cell at time t and that of the background at time t = 0, respectively, while I_{360} stands for the maximum average intensity achieved for cells that were attached to a 27-μm JP at 360 s under pulse width of 62.5 ms and 20 V. In the CFDA channel, the fluorescence intensity was normalized according to $(I_t-B_0) / (I_0-B_0) \times 100$, wherein I_t and B_0 are the areal average CFDA fluorescent intensity of the cell at time t and background at time t = 0, respectively, while I_0 stands for the initial t = 0 of the CFDA average intensity of the cell under measurement.

Numerical Simulations. The numerical simulation used to qualitatively verify the presence of asymmetric electric field gradients, arising from the proximity of a JP to a conducting wall, was performed in COMSOL 5.3. A simple two-dimensional geometry, consisting of a rectangular channel (50 μm height and 100 μm width), with a 10-μm diameter circle placed 300 nm above the substrate, was used to model the experimental setup. Since the electric double layers (EDLs) (λ) are thin, relative to the radius (a) of the particle (λ/a ≪ 1), the Laplace equation can be solved for the electric potential, ϕ, in conjunction with the following boundary condition at the metallic side of the JP:

$$\sigma\frac{\partial\phi}{\partial n} = i\omega C_{DL}(\phi - V_{floating}),$$ [1]

which describes the oscillatory Ohmic charging of the induced EDL, wherein $V_{floating}$ is the floating potential of the metallic hemisphere of the JP, n is the coordinate in the direction normal to the JP surface, and C_{DL} represents the capacitance per unit area of the EDL and can be estimated from the Debye–Hückel theory, as $C_{DL} = \varepsilon/\lambda$. In addition, a floating boundary condition (43) was applied on the metallic hemisphere so as to obey total zero charge. An insulation boundary condition was applied on the dielectric hemisphere of the JP, a voltage of 6.25 V was applied at the lower substrate (y = 0), while the upper wall was grounded, and the edges of the channel were assigned an insulating boundary condition.

Calculation of the Transmembrane Potential. The Schwan's equation (71) was used to approximate the transmembrane potential of the K562 cell:

$$\Delta\psi_{membr} = 1.5aE_{appl}\cos\theta \Big/ \left[1 + (\omega\tau)^2\right]^{1/2},$$ [2]

$$\tau = aC_{membr}\left(\rho_{int} + \frac{\rho_{ext}}{2}\right),$$ [3]

where θ is the angle between the electric field direction and the normal to the cell membrane, E_{appl} is the applied field strength, f is the frequency, $\omega = 2\pi f$ is the angular frequency, a is the radius of the cell, C_{membr} (F/cm^2) is the capacitance of the membrane, ρ_{int} is the resistivity of the internal fluid, ρ_{ext} is the resistivity of external medium, and τ is the membrane relaxation time. The transmembrane potential for K562 under various conditions is listed in Table 1.

Data Availability. All study data are included in the article and/or *SI Appendix*.

1. M. Golzio, J. Teissié, M.-P. Rols, Direct visualization at the single-cell level of electrically mediated gene delivery. *Proc. Natl. Acad. Sci. U.S.A.* **99**, 1292–1297 (2002).
2. S. I. Sukharev, V. A. Klenchin, S. M. Serov, L. V. Chernomordik, C. YuA, Electroporation and electrophoretic DNA transfer into cells. The effect of DNA interaction with electropores. *Biophys. J.* **63**, 1320–1327 (1992).
3. T. DiTommaso et al., Cell engineering with microfluidic squeezing preserves functionality of primary immune cells in vivo. *Proc. Natl. Acad. Sci. U.S.A.* **115**, E10907–E10914 (2018).
4. M. Emerson et al., Transfection efficiency and toxicity following delivery of naked plasmid DNA and cationic lipid-DNA complexes to ovine lung segments. *Mol. Ther.* **8**, 646–653 (2003).
5. S. Basiouni, H. Fuhrmann, J. Schumann, High-efficiency transfection of suspension cell lines. *Biotechniques* **53**, 1–4 (2012).
6. G. Chu, H. Hayakawa, P. Berg, Electroporation for the efficient transfection of mammalian cells with DNA. *Nucleic Acids Res.* **15**, 1311–1326 (1987).
7. E. Neumann, M. Schaefer-Ridder, Y. Wang, P. H. Hofschneider, Gene transfer into mouse lyoma cells by electroporation in high electric fields. *EMBO J.* **1**, 841–845 (1982).
8. M. P. Stewart et al., In vitro and ex vivo strategies for intracellular delivery. *Nature* **538**, 183–192 (2016).
9. G. L. Szeto et al., Microfluidic squeezing for intracellular antigen loading in polyclonal B-cells as cellular vaccines. *Sci. Rep.* **5**, 10276 (2015).
10. A. Sharei et al., A vector-free microfluidic platform for intracellular delivery. *Proc. Natl. Acad. Sci. U.S.A.* **110**, 2082–2087 (2013).
11. Y.-C. Wu et al., Massively parallel delivery of large cargo into mammalian cells with light pulses. *Nat. Methods* **12**, 439–444 (2015).
12. X. Xie et al., Nanostraw-electroporation system for highly efficient intracellular delivery and transfection. *ACS Nano* **7**, 4351–4358 (2013).

Wu et al.
Micromotor-based localized electroporation and gene transfection of mammalian cells

ENGINEERING

13. J. J. VanDersarl, A. M. Xu, N. A. Melosh, Nanostraws for direct fluidic intracellular access. *Nano Lett.* **12**, 3881–3886 (2012).

14. Y. Cao *et al.*, Nontoxic nanopore electroporation for effective intracellular delivery of biological macromolecules. *Proc. Natl. Acad. Sci. U.S.A.* **116**, 7899–7904 (2019).

15. X. Zhao *et al.*, Nanochannel electroporation as a platform for living cell interrogation in acute myeloid leukemia. *Adv. Sci. (Weinh.)* **2**, 1500111 (2015).

16. L. Chang *et al.*, 3D nanochannel electroporation for high-throughput cell transfection with high uniformity and dosage control. *Nanoscale* **8**, 243–252 (2016).

17. P. E. Boukany *et al.*, Nanochannel electroporation delivers precise amounts of bio-molecules into living cells. *Nat. Nanotechnol.* **6**, 747–754 (2011).

18. J. A. Lundqvist *et al.*, Altering the biochemical state of individual cultured cells and organelles with ultramicroelectrodes. *Proc. Natl. Acad. Sci. U.S.A.* **95**, 10356–10360 (1998).

19. B. P. Nadappuram *et al.*, Nanoscale tweezers for single-cell biopsies. *Nat. Nanotechnol.* **14**, 80–88 (2019).

20. W. Gao *et al.*, Artificial micromotors in the mouse's stomach: A step toward in vivo use of synthetic motors. *ACS Nano* **9**, 117–123 (2015).

21. J. Orozco *et al.*, Micromotor-based high-yielding fast oxidative detoxification of chemical threats. *Angew. Chem. Int. Ed. Engl.* **52**, 13276–13279 (2013).

22. W. Gao *et al.*, Seawater-driven magnesium based Janus micromotors for environmental remediation. *Nanoscale* **5**, 4696–4700 (2013).

23. J. Li *et al.*, Self-propelled nanomotors autonomously seek and repair cracks. *Nano Lett.* **15**, 7077–7085 (2015).

24. M. Medina-Sánchez, O. G. Schmidt, Medical microbots need better imaging and control. *Nature* **545**, 406–408 (2017).

25. A. M. Boymelgreen, T. Balli, T. Miloh, G. Yossifon, Active colloids as mobile micro-electrodes for unified label-free selective cargo transport. *Nat. Commun.* **9**, 760 (2018).

26. S. K. Srivastava, M. Medina-Sánchez, B. Koch, O. G. Schmidt, Medibots: Dual-action biogenic microdaggers for single-cell surgery and drug release. *Adv. Mater.* **28**, 832–837 (2016).

27. L. Yang *et al.*, Targeted single-cell therapeutics with magnetic tubular micromotor by one-step exposure of structured femtosecond optical vortices. *Adv. Funct. Mater.* **29**, 1905745 (2019).

28. Z. Lin *et al.*, Magnetically actuated peanut colloid motors for cell manipulation and patterning. *ACS Nano* **12**, 2539–2545 (2018).

29. H. Xu *et al.*, Sperm-hybrid micromotor for targeted drug delivery. *ACS Nano* **12**, 327–337 (2018).

30. J. Cui *et al.*, Nanomagnetic encoding of shape-morphing micromachines. *Nature* **575**, 164–168 (2019). Correction in: *Nature* **578**, E10 (2020).

31. W. Wang, Z. Wu, X. Lin, T. Si, Q. He, Gold-nanoshell-functionalized polymer nano-swimmer for photomechanical poration of single-cell membrane. *J. Am. Chem. Soc.* **141**, 6601–6608 (2019).

32. D. Ahmed *et al.*, Bio-inspired acousto-magnetic microswarm robots with upstream motility. *Nat. Mach. Intell.* **3**, 116–124 (2021).

33. Y. Alapan, B. Yigit, O. Beker, A. F. Demirörs, M. Sitti, Shape-encoded dynamic assembly of mobile micromachines. *Nat. Mater.* **18**, 1244–1251 (2019).

34. B. E.-F. de Ávila *et al.*, Micromotor-enabled active drug delivery for in vivo treatment of stomach infection. *Nat. Commun.* **8**, 1–9 (2017).

35. K. Villa *et al.*, Cooperative multifunctional self-propelled paramagnetic microrobots with chemical handles for cell manipulation and drug delivery. *Adv. Funct. Mater.* **28**, 1804343 (2018).

36. F. Zhang *et al.*, A macrophage-magnesium hybrid biomotor: Fabrication and characterization. *Adv. Mater.* **31**, e1901828 (2019).

37. C. K. Schmidt, M. Medina-Sánchez, R. J. Edmondson, O. G. Schmidt, Engineering microrobots for targeted cancer therapies from a medical perspective. *Nat. Commun.* **11**, 5618 (2020).

38. V. M. Kadiri *et al.*, Biocompatible magnetic micro- and nanodevices: Fabrication of FePt nanopropellers and cell transfection. *Adv. Mater.* **32**, e2001114 (2020).

39. F. Qiu *et al.*, Magnetic helical microswimmers functionalized with lipoplexes for targeted gene delivery. *Adv. Funct. Mater.* **25**, 1666–1671 (2015).

40. Y. Wu, A. Fu, G. Yossifon, Active particles as mobile microelectrodes for selective bacteria transport and electroporation. *Sci. Adv.* **6**, eaay4412 (2020).

41. T. Mirkovic, N. S. Zacharia, G. D. Scholes, G. A. Ozin, Nanolocomotion - Catalytic nanomotors and nanorotors. *Small* **6**, 159–167 (2010).

42. S. Gangwal, O. J. Cayre, M. Z. Bazant, O. D. Velev, Induced-charge electrophoresis of metallodielectric particles. *Phys. Rev. Lett.* **100**, 058302 (2008).

43. T. M. Squires, M. Z. Bazant, Breaking symmetries in induced-charge electro-osmosis and electrophoresis. *J. Fluid Mech.* **560**, 65–101 (2006).

44. A. Boymelgreen, G. Yossifon, T. Miloh, Propulsion of active colloids by self-induced field gradients. *Langmuir* **32**, 9540–9547 (2016).

45. Y. Wu, A. Fu, G. Yossifon, Active particle based selective transport and release of cell organelles. *Small* **16**, 1906682 (2020).

46. L. Chang *et al.*, Micro-/nanoscale electroporation. *Lab Chip* **16**, 4047–4062 (2016).

47. R. Pethig, Review article-dielectrophoresis: Status of the theory, technology, and applications. *Biomicrofluidics* **4**, 022811 (2010).

48. A. Boymelgreen, G. Yossifon, Observing electrokinetic Janus particle-channel wall interaction using microparticle image velocimetry. *Langmuir* **31**, 8243–8250 (2015).

49. Y. Wu, A. Fu, G. Yossifon, Active particles as mobile microelectrodes for selective bacteria electroporation and transport. *Sci. Adv.* **6**, eaay4412 (2020).

50. G. Pucihar, T. Kotnik, M. Kandušer, D. Miklavčič, The influence of medium conductivity on electropermeabilization and survival of cells in vitro. *Bioelectrochemistry* **54**, 107–115 (2001). Correction in: *Bioelectrochemistry* **58**, 203 (2002).

51. C. S. Djuzenova *et al.*, Effect of medium conductivity and composition on the uptake of propidium iodide into electropermeabilized myeloma cells. *Biochim. Biophys. Acta* **1284**, 143–152 (1996).

52. K. J. Müller, V. L. Sukhorukov, U. Zimmermann, Reversible electropermeabilization of mammalian cells by high-intensity, ultra-short pulses of submicrosecond duration. *J. Membr. Biol.* **184**, 161–170 (2001).

53. M. Pavlin, D. Miklavčič, Theoretical and experimental analysis of conductivity, ion diffusion and molecular transport during cell electroporation—Relation between short-lived and long-lived pores. *Bioelectrochemistry* **74**, 38–46 (2008).

54. B. C. Brambach, A. Michels, J. Franzke, R. Kettler, Current density and conductivity dependent electroporation of *Escherichia coli* C600. *Prog. Biophys. Mol. Biol.* **111**, 46–54 (2013).

55. S. Wang, L. J. Lee, Micro-/nanofluidics based cell electroporation. *Biomicrofluidics* **7**, 11301 (2013).

56. V. F. I. Van Tendeloo *et al.*, Highly efficient gene delivery by mRNA electroporation in human hematopoietic cells: Superiority to lipofection and passive pulsing of mRNA and to electroporation of plasmid cDNA for tumor antigen loading of dendritic cells. *Blood* **98**, 49–56 (2001).

57. Y. Zu, X. Liu, A.-Y. Chang, S. Wang, Flow micropillar array electroporation to enhance size specific transfection to a large population of cells. *Bioelectrochemistry* **132**, 107417 (2020).

58. S. Wang, X. Zhang, W. Wang, L. J. Lee, Semicontinuous flow electroporation chip for high-throughput transfection on mammalian cells. *Anal. Chem.* **81**, 4414–4421 (2009).

59. A.-Y. Chang *et al.*, Microfluidic electroporation coupling pulses of nanoseconds and milliseconds to facilitate rapid uptake and enhanced expression of DNA in cell therapy. *Sci. Rep.* **10**, 6061 (2020).

60. S. Liebscher, M. Meyer-Luehmann, A peephole into the brain: Neuropathological features of Alzheimer's disease revealed by in vivo two-photon imaging. *Front. Psychiatry* **3**, 26 (2012).

61. L. A. Volpicelli-Daley *et al.*, Formation of α-synuclein Lewy neurite-like aggregates in axons impedes the transport of distinct endosomes. *Mol. Biol. Cell* **25**, 4010–4023 (2014).

62. K. R. Weiss, Y. Kimura, W.-C. M. Lee, J. T. Littleton, Huntingtin aggregation kinetics and their pathological role in a Drosophila Huntington's disease model. *Genetics* **190**, 581–600 (2012).

63. Z. Li *et al.*, Allele-selective lowering of mutant HTT protein by HTT-LC3 linker compounds. *Nature* **575**, 203–209 (2019).

64. R. Mhanna *et al.*, Artificial bacterial flagella for remote-controlled targeted single-cell drug delivery. *Small* **10**, 1953–1957 (2014).

65. X. Xu *et al.*, Precision-guided nanospears for targeted and high-throughput intracellular gene delivery. *ACS Nano* **12**, 4503–4511 (2018).

66. D. J. Bakewell, H. Morgan, Dielectrophoresis of DNA: Time- and frequency-dependent collections on microelectrodes. *IEEE Trans. Nanobioscience* **5**, 1–8 (2006).

67. S. Tuukkanen *et al.*, Trapping of 27 bp-8 kbp DNA and immobilization of thiol-modified DNA using dielectrophoresis. *Nanotechnology* **18**, 295204 (2007).

68. P. V. Jones, G. L. Salmon, A. Ros, Continuous separation of DNA molecules by size using insulator-based dielectrophoresis. *Anal. Chem.* **89**, 1531–1539 (2017).

69. R. Pethig, Review—Where is dielectrophoresis (DEP) going? *J. Electrochem. Soc.* **164**, B3049–B3055 (2017).

70. C.-Y. Wu, K. T. Roybal, E. M. Puchner, J. Onuffer, W. A. Lim, Remote control of therapeutic T cells through a small molecule-gated chimeric receptor. *Science* **350**, aab4077 (2015).

71. P. Marszalek, D. S. Liu, T. Y. Tsong, Schwan equation and transmembrane potential induced by alternating electric field. *Biophys. J.* **58**, 1053–1058 (1990).

www.manaraa.com